*Article*

# A Digitalized Methodology for Co-Design Structural and Performance Optimization of Battery Modules †

**Theodoros Kalogiannis \*** , **Md Sazzad Hosen, Joeri Van Mierlo, Peter Van Den Bossche and Maitane Berecibar**

Battery Innovation Centre, MOBI Research Group, Vrije Universiteit Brussel (VUB), Pleinlaan 2, 1050 Brussel, Belgium; md.sazzad.hosen@vub.be (M.S.H.); joeri.van.mierlo@vub.be (J.V.M.); peter.van.den.bossche@vub.be (P.V.D.B.); maitane.berecibar@vub.be (M.B.)
\* Correspondence: theodoros.kalogiannis@vub.be
† Paper Presented at EVS36 the 36th International Electric Vehicle Symposium and Exhibition, Sacramento, CA, USA, 11–14 June 2023.

**Abstract:** In this study, we present an innovative, fully automated, and digitalized methodology to optimize the energy efficiency and cost effectiveness of Li-ion battery modules. Advancing on from today's optimization schemes that rely on user experience and other limitations, the mechanical and thermal designs are optimized simultaneously in this study by coupling 3D multi-physical behavior models to multi-objective heuristic optimization algorithms. Heat generation at various loading and ambient conditions are estimated with a physics-based, fractional-order battery cell-level model, which is extrapolated to a module that further accounts for the interconnected cells' heat transfer phenomena. Several key performance indicators such as the surface temperature increase, the temperature variations on the cells, and heat uniformity within the module are recorded. For the air-cooled study case, the proposed coupled framework performs more than 250 module evaluations in a relatively short time for the whole available electro-thermal-mechanical design space, thereby ensuring global optimal results in the final design. The optimal module design proposed by this method is built in this work, and it is experimentally evaluated with a module composed of 12 series-connected Li-ion NMC/C 43Ah prismatic battery cells. The performance is validated at various conditions, which is achieved by accounting the thermal efficiency and pressure drop with regard to power consumption improvements. The validations presented in this study verify the applicability and overall efficiency of the proposed methodology, as well as paves the way toward better energy and cost-efficient battery systems.

**Keywords:** lithium-ion; electro-thermal model; battery thermal management; multi-physics and multi-objective optimization; particle swarm optimization; energy storage; structural design; battery module

## 1. Introduction

Currently, lithium-ion batteries (Li-ion) are utilized in many electro-motive applications and in grid support due to their good operating efficiency and lifetimes [1,2], and they are also used in attempts to reduce greenhouse emissions, as well as in attempts to transition from the fossil fuel era [3,4]. Nonetheless, to obtain the optimal performance of Li-ion cells, they have to be monitored and preserved within a safe operating area (SoA) [5]. The thermal, safe-operating window is defined by the manufacturer according to the cell's chemistry and shape. Moreover, it depends on the current rate and it is usually between 20 °C to 40 °C [6]. For multi-cell designs, the cell-to-cell interactions, enclosure shields, and high-power demands (e.g., fast charge) can increase the cells' temperature or create heat non-uniformities with severe safety and performance implications. Hence, a battery thermal management system (BTMS) is always utilized to maintain a predefined SoA [7,8].

Various approaches for a BTMS can be found in the literature and in real-life applications, and they are categorized based on thermal resistance (direct/indirect cooling/heating

inter-phase) or the cooling mediums (water-based/dielectric/air/phase-change, etc.) that are implemented in electric vehicles to preserve the temperature. In addition, they are typically tailor based, and they are used to account for low costs, good performance, scalability, modularity, etc. [9,10]. Many studies have been carried out that have evaluated and optimized air-based cooling BTMSs [11]. The air cooling module is the simplest in terms of mechanical and thermal design, and it was selected in this study for a proof-of-concept of our proposed methodology; however, it was also used without limiting the proposed method to air-based applications.

In [12], the optimal configuration of a battery pack composed of cylindrical Li-ion cells was proposed, whereby the authors showed that a cell arrangement with a small length-width ratio, in addition to an inlet/outlet configuration that facilitates the air flow over most of cells, can significantly improve cooling efficiency. Park [13] evaluated several air-cooled BTMS designs for Li-ion cells by theoretical investigations on a proposed numerical model. The aforementioned author showed that BTMS efficiency is highly dependent on the uniform distribution of the air passage, which can be achieved by adding a tapered manifold and pressure relief ventilation to the BTMS.

Chen et al. [14] proposed a flow resistance network model to capture the friction pressure loss along the BTMS channel, which was seen as the frictions between air and channel wall in air-based BTMSs. By these means, they calculated the velocities of the cooling channels and modeled the heat transfer and temperature distribution of the battery cells. The coupling of these models showed improvements in the thermal management efficiency of the BTMSs. Optimization of the air-cooled modules was also performed in [15], where tje authors investigated the influence of the air inlet/outlet angles and the width of the air flow channels between the battery cells. Similar assessments were performed in [16] for both a U-type and Z-type air-based BTMS, where it was also concluded that the cooling efficiency and power consumption can be improved by optimizing the aforementioned parameters. Moreover, experimental and numerical evaluations on air-cooled BTMSs were performed in [17]. Those authors investigated various performance parameters, such as the channel size, channel locations, mass flow rates, and temperature influence, and they calculated the pressure drop during constant current operation. They proposed a J-type BTMS by integrating the Z- and U-type designs, as well as by means of surrogate modeling, and through this approach they optimized the heat distribution in the battery module.

In order to estimate the optimal channel position on air-cooled BTMSs, the authors in [18] investigated several BTMS types with different input and output channels topologies, albeit with the same design parameters such as cell spacing, channel size, air flow rate, and temperature. They performed a numerical study on various designs and concluded that the cooling efficiency was improved if the channel regions were in the middle of the plenums. Li et al. [19] evaluated the effect of the manifold size and mass flow rate on a U-type Li-ion module that was composed of 36 battery cells. The authors of the current study concluded that increasing the channel size of the mass flow rate can deteriorate the temperature uniformity of the cells; in addition, an optimization was suggested to balance the air flow density and rate with the cell-to-cell variations and energy cost.

Among the research that has been already performed in the field, to the best of our knowledge, there has been limited information presented on performing co-design optimizations with a combination of multi-objective and multi-physics models.

Hence, in this study, we investigated the modeling capabilities of a physics-based, fractional-order electro-thermal model that was coupled to a 3D multi-physics module model. This model was used to evaluate the cooling performance of a proposed optimized BTMS, which was composed of 12 Li-ion prismatic cells. The methodology was initially presented in our previous study [20], where the optimized battery module was compared to the baseline model. The selected solutions of the co-design optimization model were thoroughly presented and evaluated, and this was achieved by taking into account the multi-objective optimization methods presented here [21] without the performance of laboratory assessments on the developed battery modules.

In this work, the design space from the optimization was built and evaluated to bring validity to our proposed methodology. The findings from [20] indicated that, over a broad design space with various parameters to account for (i.e., geometrical and performance indicators), a unique battery module design can be selected. Meanwhile, from over 250 structural and performance investigations, the algorithm was able to propose a single battery module that simultaneously minimizes all the selected objectives.

In this paper, we built the proposed battery module in our labs, and we tested it with various current profiles for functional assessments. A detailed comparison between the experimental and modeling performance was further performed to assess and validate the proposed design optimization methodology. Moreover, we performed a second step optimization study to evaluate and maximize the cost effectiveness of the proposed methodology. In this work, we evaluated the performance with both static and dynamic loading profiles to generate various heat profiles on the battery cells and modules.

Three cases were utilized to assess the applicability of the method, i.e., high heat-generation static currents, a conventional discharge/charge cycle, and a dynamic loading profile, according to the worldwide harmonized light vehicle test procedure (WLTP). Once the single cell and the module models were validated, the proposed BTMS was strategically optimized to balance between the temperature management and pressure drop, which was achieved by exploring various mass flow rates, inlet/outlet channel sizes, and geometrical parameters.

The introduction is followed by Section 2, in which the experimental methodology is described. Thereafter, we have Section 3, which details the single cell physics-based model and multi-cell module model development. In Section 4, the electro-thermal experimental validation is performed at three loading conditions. Section 5 details the numerical optimization that was conducted on the proposed air-cooled BTMS. Lastly, in Section 7, the paper is concluded and a discussion on future steps is conducted.

## 2. Experimental Setup

### 2.1. Li-Ion Cell Properties

A prismatic NMC/C lithium-ion cell was used in this study, as shown in Figure 1. The cell was designed for high-energy applications with a nominal capacity at 43 Ah, and it is capable of a current rate (C-rate or C) of up to a 2C constant loading.



|          (**a**)          |          (**b**)          |
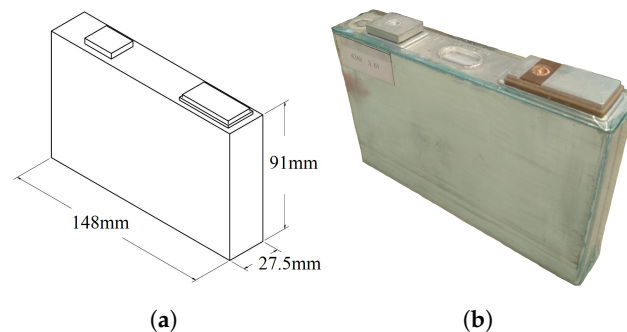
**Figure 1.** (**a**) CAD cell design. (**b**) The actual NMC/C prismatic cell.

The main electrical and mechanical parameters of the Li-ion prismatic cell used in this study are displayed in Table 1.

**Table 1.** Electro-mechanical properties of the Li-ion cell.

| Main Characteristics | Value | Unit |
|:---:|:---:|:---:|
| Chemistry | NMC/C | (-) |
| Shape | Prismatic | (-) |
| Nominal voltage | 3.65 | (V) |
| Nominal capacity * | 43 | (Ah) |

**Table 1.** *Cont.*

| Main Characteristics | Value | Unit |
|---|---|---|
| End-of-charge maximum voltage | 4.2 | (V) |
| End-of-discharge cut-off voltage | 3 | (V) |
| Volumetric energy density * | 424 | (Wh/L) |
| Specific energy density * | 186.8 | (Wh/kg) |
| Specific power * | >1200 | (W/kg) |
| AC impedance (1 kHz) | <1 | (mOhms) |
| Recommended charge current rate (continuous) * | 1 C | (-) |
| Maximum charge C-rate | 2 C | (-) |
| Cell dimensions | $148 \times 91 \times 27.5$ | (mm) |
| Positive tab | $6 \times 18 \times 22$ | (mm) |
| Negative tab | $6 \times 18 \times 38$ | (mm) |
| Weight | 0.840 | (kg) |

* At 1 C and 25 °C.

## 2.2. BTMS Configuration

A Z-type BTMS with parallel air flow to the cells is proposed in this study. Figure 2 shows the design configuration of the proposed air-cooled BTMS.
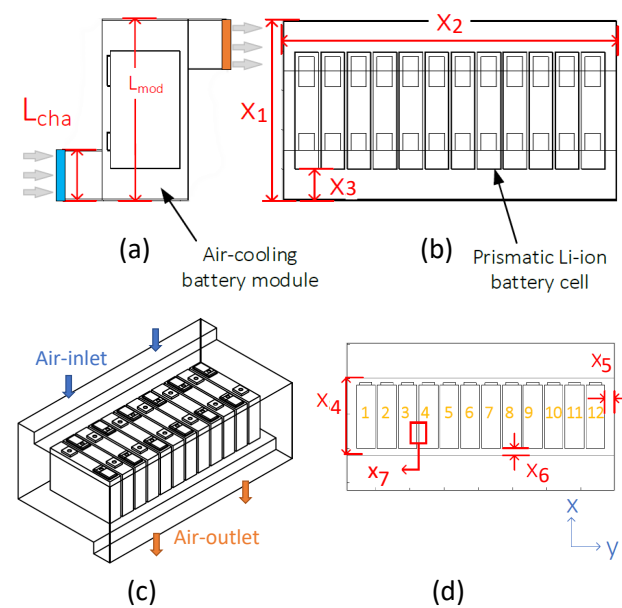


**Figure 2.** (**a**) Side view. (**b**) Top view. (**c**) The proposed BTMS inlet/outlet channels. (**d**) The BTMS cell configurations with the cells placed in the module (cell 1 to cell 12).

In Figure 2a, the inlet/outlet orientation and size is shown; in this study, this is denoted as $L_{cha}$, and it is approximately equal to a third over the total channel's area, which is denoted as $L_{mod}$. The inlet and outlet channels are, respectively, represented by blue and orange colors. In Figure 2b, the top view of the BTMS is shown, with the BTMS total length and width dimensions being denoted as $x_1$ and $x_2$, respectively. Meanwhile, $x_3$ represents the space from the cells to the BTMS's side wall. In Figure 2c, the proposed Z-type parallel-flow BTMS is shown with air inlet and outlet channels, whereas Figure 2d shows the internal configuration of the cells with respect to the BTMS boundaries, where $x_4$ is the height of the BTMS; $x_5$ and $x_6$ are the distances between the outer cells to the x- and y-axis side walls, respectively; and $x_7$ is the cell-to-cell distance. Lastly, it should be noted that the symmetries for all sides were considered. The proposed dimensions for the implementation of the BTMS were gathered and are shown in Table 2.

**Table 2.** Mechanical parameters of the proposed air-based BTMS.

| Main Parameter | Implemented Value | Unit |
|---|---|---|
| $x_1$ | 201.2 | (mm) |
| $x_2$ | 412.9 | (mm) |
| $x_3$ | 26.6 | (mm) |
| $x_4$ | 152.6 | (mm) |
| $x_5$ | 20 | (mm) |
| $x_6$ | 30.8 | (mm) |
| $x_7$ | 3.9 | (mm) |

*2.3. Test Bench*

For the implementation of the BTMS, we initially electro-thermally characterized the prismatic cell. The electrical process included the capacity test that was conducted to obtain the actual cell's value at various temperatures and current rates. Also, it included impedance measurements, which were performed with the hybrid pulse power test (HPPC), as well as with measurements, to obtain the open-circuit voltage of the cells at different states of charges (SoCs). The raw data obtained from the tests were used to map the proposed modeling behavior. A particle swarm optimization (PSO) was utilized to extract the model parameters, the detailed experimental characterization process of which can be found in [22]. The cooling efficiency of a BTMS is often described with the maximum temperature ($T_{max}$), the temperature difference among the cells ($DT$), the temperature difference on the cell surface ($Cell_T$), and the total volume ($V$) that the battery module occupies. The primal objective, serving as an attempt through which to improve the volumetric and gravimetric energy densities of the modules, is to keep the cells within a safe operation temperature area but simultaneously minimize the volume or the weight. The significance of these KPIs is related to temperature management, which plays a crucial role in assessing the safety, reliability, and efficiency of Li-ion batteries. The maximum temperature rise observed on the outer casing or surface of the various form factors or formats during its operation is referred to as surface temperature increase ($T_{max}$). Elevated levels may signal operational inefficiencies, including internal resistance rise, poor power capabilities, overcharging, or excessive current consumption. These inefficiencies could serve as early warning signs of thermal runaway, which is a dangerous scenario characterized by a rapid escalation in battery temperature that could potentially result in the venting, fire, or explosion of the cells. The temperature difference ($DT$) among the cells is also referred as thermal uniformity in a multi-cell topology. Non-uniform temperature distribution can lead to localized hotspots, which accelerate degradation and reduce the overall lifespan of the battery. Monitoring temperature variations helps in identifying potential thermal management issues, such as poor heat dissipation, uneven cooling, or cell-to-cell variations in performance. Last but not least, the temperature difference on the cell surface ($Cell_T$) indicates the heat generation from the core of the cells to the outer casing, which can lead to uneven heat distribution and to local hot spots that affect the efficiency and reliability of Li-ion batteries (as it induces thermal stress on individual cells and increases the risks of thermal runaway).

In this method, the objective of the algorithm was defined so as to minimize these four parameters, and this was achieved by taking into account the complex multi-variable and multi-physical requirements of the design. The multi-objective particle swarm optimization algorithm (MOPSO) was developed in MATLAB (and was published in our previous work [21]). It is linked here to the 3D model created in Comsol to solve the multidisciplinary costs, which can mathematically be expressed as in Equation (1):

$$\min_i F(x_i) = \left[ T_{max}^i, DT^i, Cell_T^i, V^i \right], \forall i = 1 \le x_9 \le 9$$
$$s.t. = [x_1, x_2, x_3, x_4, x_5, x_6, x_7, x_8]$$
$$at \left[ v, C_r, T_{amb}, v_{temp} \right]. \tag{1}$$

The mass flow rate $v$ will be further examined in this work as a second-optimization step that accounts for cost efficiency.

The thermal properties of the cell were found with a micro-pulse heat profile that was injected into the cell, whereby the same number of Ah was extracted and injected in order to be SoC-independent, which could result in influencing electrical and thermal parameters such as the cells' resistances. The extracted specific heat and the convection transfer coefficient were found in our previous work [23]. Once the cells were characterized, the module development took place, which was based on the optimized selected geometry presented in Table 2. For the 12S1P module implementation, an electrical characterization of more than 100 cells was performed to select the ones with the closest values in a Ragone plot in terms of capacity and impedance. A variation of up to 3% and 11% was exhibited at the beginning of life (BoL) and at the same testing conditions, respectively. A total of 12 cells were selected that showed similar performance in terms of cycle capacity and impedance at the various conditions, whereas the BTMS design that was implemented was based on BTMS 5, which showed—in simulation—a potential 15% decrease in the maximum temperature increase on the cells, a 5% decrease in the required volume, a 70% decrease in the temperature uniformity among the cells, and approximately a 40% decrease in the better heat distribution on a cell [20]. The selected battery module was constructed with a plexi glass that iwass precisely manufactured to follow the optimized dimensions. In addition, three fans were placed in the proposed inlet location with a variable mass flow rate and power consumption. The battery module was placed in a room with a control ambient temperature at 25 °C and a specific convection rate.

The hardware setup for the testing included a climate chamber to preserve the cells' surface temperatures, which were close to the various environmental conditions. The single cells were connected to a PEC ACT0550 tester, (PEC, Leuven, Belgium) which is capable of up to DC 5 V measurements. In addition, the module was connected to a PEC SBT8050, which is capable of up to 80 V DC. Both of the testers had a ±0.005% voltage accuracy. The module was connected to a pre-charge circuit and a fuse relay safety box, and it was monitored by a commercially available battery management system (BMS). An anemometer and a temperature data logger were used to measure the mass flow rates and to obtain the cells' surface temperatures in the module. The overall test bench is shown in Figure 3, where the green and blue paths indicate the cell and module level testing, respectively.
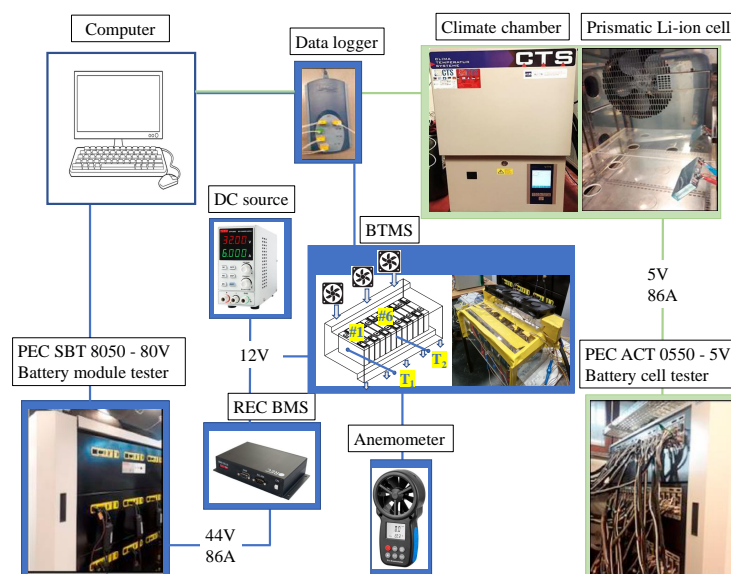


**Figure 3.** Experimental setup during the cell- (green) and module-level (blue) characterizations and validations.

### 3. Model Development

Physically meaningful battery models can be employed by means of differential equations and fractional order calculus (FOC), where the lumped capacitor of the ECM [22] is replaced with constant phase elements (CPE), which can greatly improve the modeling accuracy [24,25]. A Thevenin FOC model was presented in [26] that can achieve significant improvements on its electrical behavior compared to an empirical model. The modeling impedance was correlated to the actual cells by way of comparisons to the electrochemical impedance spectroscopy (EIS) results at various cell aging states. Several FOC models can be found in the literature. However, the Thevenin equivalent with a current dependency on a charge transfer resistance that is based on the Butler–Volmer approximation (BVE) [27] combined with a diffusion element (Warburg) [28] has shown a good performance and balance between computational burden and accuracy. An R-(BVE//CPE)-W FOC coupled to a thermal model is thus proposed in this study.

*3.1. The Physics-Based FOC Electro-Thermal Model*

3.1.1. Electrical Part

The FOC model describes the impedance behavior according to the CPE elements, as expressed in Equation (2):

$$Z_{CPE}(f) = \frac{1}{Q(j2\pi f)^{\alpha}}, (0 < \alpha < 1),$$  (2)

where $j$ is the imaginary part, and $\alpha$ and $Q$ are the variables used to obtain the CPE. An ideal capacitor can be represented in case $\alpha$ is equal to 1; when $\alpha$ is equal to 0, it is instead treated as a pure resistor. Moreover, $\alpha$ can be obtained directly from the EIS measurements [29], or it can be numerically calculated with FOC calculus, where the real-order differential operator can be defined as in Equation (3):

$$_{\alpha}\mathcal{D}_{t}^{\alpha} = \begin{cases} \frac{d^{\alpha}}{dt^{\alpha}}, & \alpha > 0 \\ 1, & \alpha = 0 \\ \int\limits_{\alpha}^{t} (d\tau)^{\alpha}, & \alpha < 0, \end{cases}$$  (3)

where the fractional order in a real domain is denoted as $\alpha$. The discrete form of the FOC can be numerically solved according to the Grünwald–Letnikov (GL) definition in fractional calculus [30]:

$$\mathcal{D}^{\alpha}f(t) = \lim_{\Delta t \to 0} \frac{1}{(\Delta t)^{\alpha}} \sum_{j=0}^{[t/\Delta t]} (-1)^{j} \binom{\alpha}{j} f(t - j\Delta t),$$  (4)

where the sampling time is represented with $\Delta t$; the user-defined memory length is denoted as $[t/\Delta t]$; and $\binom{\alpha}{j}$ is the Newton binomial coefficient, which is calculated as in Equation (5):

$$\binom{\alpha}{j} = \begin{cases} 1, & j = 0 \\ \frac{\alpha!}{j!(\alpha-j)!} = \frac{\Gamma(\alpha+1)}{\Gamma(j+1)\Gamma(\alpha-j+1)}, & j > 0. \end{cases}$$  (5)

The proposed FOC model was depicted based on Kirchhoff's voltage law in accordance with the following expressions:

$$\begin{cases} U_{batt} &= V_{OC} - \eta_{Ohmic} - \eta_{ct} - \eta_{diff} \\ U_{batt} &= f(C_{r}, SoC, \theta) \\ \mathcal{D}^{\alpha}\eta_{ct} &= \frac{I_{batt}}{Q_{ct}} - \frac{\eta_{ct}}{Q_{ct}R_{BVE}} \\ \mathcal{D}^{\beta}\eta_{diff} &= \frac{1}{Q_{diff}}\eta_{diff}, \end{cases}$$  (6)

where $V_{OC}$ represents the open-circuit voltage of the cells; $\eta_{Ohmic}$ is the voltage drop of the Ohmic resistance; and $\eta_{ct}$ and $\eta_{diff}$ represent the voltage across the CPE and diffusion elements, respectively. The terminal voltage of the cell is denoted as $U_{batt}$ and is dependent on the SoC, current rates ($C_r$), and temperature ($\theta$). The fractional orders $\alpha$ and $\beta$ were assigned to the CPE elements for the polarization effects with factors $Q_{ct}$ and $Q_{diff}$, respectively. $R_{BVE}$ shows the activation polarization resistance, which was based on BVE approximation [31,32].

$$R_{BVE,s} = \alpha_{0,s} \cdot \frac{ln\left[\frac{1}{\alpha_{1,s}}I_{batt,s} + \sqrt{\left(\frac{1}{\alpha_{1,s}}I_{batt,s}\right)^2 + 1}\right]}{\frac{1}{\alpha_{1,s}}I_{batt,s}} \tag{7}$$

where $s$ is the SoC counterl $\alpha_{0,s}$ and $\alpha_{1,s}$ are fitting parameters; and $I_{batt,s}$ is the current passing through the cell at every sample. In using the GL from Equations (3) and (4), we obtain the following transformations (Equations (8) and (9)):

$$\mathcal{D}^{\alpha}\eta_{ct} = \frac{1}{T_s^{\alpha}}\sum_{j=0}^{[k]}(-1)^j\binom{\alpha}{j}\eta_{ct,k-j} = \frac{I_{batt,k}}{Q_{ct,k}} - \frac{\eta_{ct,k}}{Q_{ct,k}R_{BVE,k}}, \tag{8}$$

$$\mathcal{D}^{\beta}\eta_{diff} = \frac{1}{T_s^{\beta}}\sum_{j=0}^{[k]}(-1)^j\binom{\beta}{j}\eta_{diff,k-j} = \frac{1}{Q_{diff,k}}\eta_{diff,k}, \tag{9}$$

where $k$ is the time step. The solutions of these two formulas were derived from the battery voltage $U_{batt}$ at the discrete time domain, as in Equation (10):

$$U_{batt,k} = V_{OC,k} - \eta_{Ohmic,k} - \eta_{ct,k} - \eta_{diff,k}, \tag{10}$$

where the corresponding voltage drops are calculated as (Equations (11)–(13))

$$\eta_{Ohmic,k} = I_{batt,k-1}R_{Ohmic}, \tag{11}$$

$$\begin{aligned}\eta_{ct,k} = &\left(\alpha - \frac{T_s^{\alpha}}{Q_{ct}R_{BVE}}\right)\eta_{ct,k-1}\\ &+ \frac{T_s^{\alpha}I_{batt,k-1}}{Q_{ct}} - \sum_{j=2}^{[N_s]}(-1)^j\binom{\alpha}{j}\eta_{ct,k-j},\end{aligned} \tag{12}$$

$$\eta_{diff,k} = \frac{T_s^{\beta}I_{batt,k-1}}{Q_{diff}} - \frac{1}{T_s^{\beta}}\sum_{j=0}^{[N_s]}(-1)^j\binom{\beta}{j}\eta_{diff,k-j}. \tag{13}$$

### 3.1.2. Thermal Part

For the thermal branch, and in order to obtain the heat dissipation rates, the temperature gradient was calculated as in Equation (14) [33]:

$$\begin{cases}\frac{dU_{cell}}{dt} = Q_{gen}(t) - Q_{loss}(t) = m\,C_p\,\frac{dT}{dt}\\ Q_{loss}(t) = Q_{conv}(t),\end{cases} \tag{14}$$

where $U_{cell}$ represents the internal energy of the Li-ion and $Q_{gen}$ is the generated heat rate based on the cell's Joule losses. $Q_{loss}$ represents the heat loss expressed by the convective heat transfer to the environment. Also, $m$ is the cell mass, $C_p$ is the heat capacity, and $T$ is

the surface temperature. The heat transfer to the ambient temperature was calculated as shown in Equation (15):

$$\begin{cases} Q_{gen}(C_r, SoC, \theta) &= R_{Ohmic}(C_r, SoC, \theta) \, I_{batt}^2 \\ &\quad + R_{BVE}(C_r, SoC, \theta) \, I_{ct}^2 \\ Q_{loss}(C_r, SoC, \theta) &= h_{conv} S (T_{amb} - T_{cell}), \end{cases} \tag{15}$$

### 3.1.3. Coupled Electro-Thermal Model

Where $h_{conv}$ is the cell-level convection heat transfer coefficient and S is the cell cross-section area. The thermal properties of the model were calculated in our previous work [23]. Figure 4 shows the coupled 1D electro-thermal model.

(**a**)

(**b**)

(**c**)
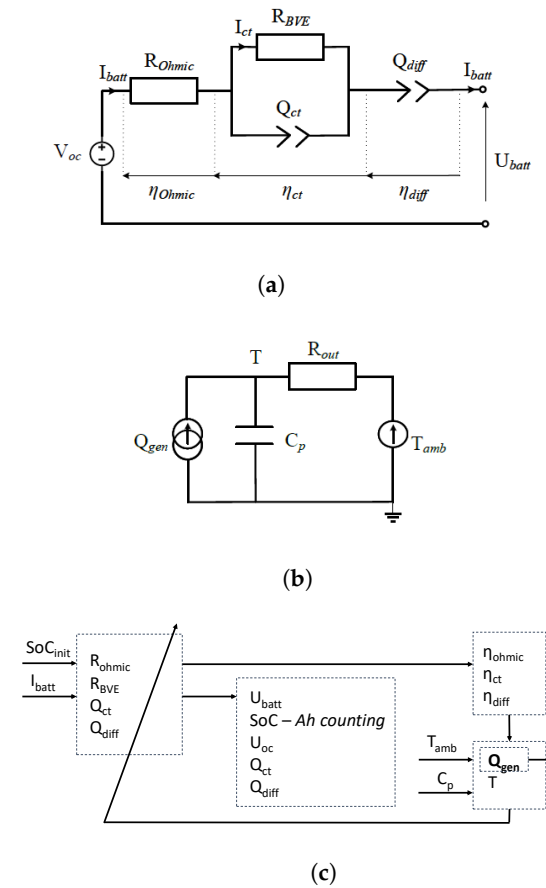
**Figure 4.** (**a**) The electrical FOC model. (**b**) The thermal branch (**c**) The coupling of the electrical FOC with the thermal 1D model.

### 3.2. 3D Numerical Model

The proposed 1D electro-thermal model derived the heat losses of the cell over time, which were fed to the 3D model as an input to further evaluate the temperature gradients at the module level. The 3D models' thermal properties, such as conductivity, cell density, and specific heat, were obtained from a characterization process that was presented in our previous work [23], whereas the rest domain parameters were found in the literature from the study of [34], and they are gathered in Table 3.

**Table 3.** Input parameters of the multi-physics model.

| Main Parameter | Air [34] | NMC/C [23] | Aluminum Tabs [34] |
|---|---|---|---|
| Density $\rho$ (kg/m$^3$) | 1.165 | 2268 | 2700 |
| Specific heat $C_p$ (J/kg·K) | 1005 | 933.7 | 900 |
| Thermal conductivity $\lambda$ (W/m·K) | 0.0267 | 0.82 ($\lambda_x$) 4.43 ($\lambda_y$) 2.72 ($\lambda_w$) | 238 |
| Electrical resistance $R'$ ($\Omega$) | | | $9.97 \times 10^{-6}$ |

The model was developed with a COMSOL computational fluid dynamics (CFDs) simulation tool, whereas the temperature and fluid fields were solved with a finite element method. We used a turbulent, single-phase, and incompressible fluid, the mass, momentum, and energy conservation of which were described according to the Reynolds average Navier–Strokes equations with a *k-ε* turbulence model [34,35] for the air flow area (Equations (16)–(18)) and the battery cells (Equation (19)):

$$\frac{\vartheta \rho_f}{\vartheta t} + \nabla \cdot \left( \rho_f \bar{v} \right) = 0, \tag{16}$$

$$\rho_f \frac{\vartheta \bar{v}}{\vartheta t} + \rho_f \left( \vec{v} \cdot \nabla \right) \bar{v} = \nabla \bar{p} + [\nabla \cdot (\mu \nabla \bar{v}) - \phi], \tag{17}$$

$$\rho_f C_p \frac{\vartheta T_f}{\vartheta t} + \left( \rho_f C_p \vec{v} \right) \nabla T_f = \nabla \cdot \left[ \left( \lambda_a + \frac{\mu_t}{\sigma_t} \right) \nabla T_f \right], \tag{18}$$

$$\rho_c C_p, c \frac{\vartheta T_c}{\vartheta t} = \nabla \cdot \left[ \vec{\lambda_c} \nabla T_c \right] + \dot{Q}_{gen} + \dot{Q}_{tab}, \tag{19}$$

where $\rho_f$ represents the fluid density; $\bar{v}$ shows the average velocity; and the viscosity, pressure, and Reynolds stress are denoted by $\mu$, $p$, and $\phi$, respectively. Also, the time-dependent heat dissipation created an unsteady temperature in the airfield region, which is described by Equation (18). In this case, the fluid temperature is denoted as $T_f$, the thermal conductivity of air is $\lambda_a$, and $\mu_t$ is the turbulent dynamic viscosity. The temperature equation for the battery module is described in Equation (19), with $\rho_c$, $C_p$, $c$, and $T_c$ the cell's density, specific heat, and surface temperature, respectively, and where $\vec{\lambda_c}$ is the thermal conductivity at each direction.

The heat generation included the losses generated from the aluminum cell's tabs in accordance with the following formula:

$$Q_{tab} = \frac{R' \cdot I_{batt}^2}{Vl_{tab}} * N, \tag{20}$$

where N is the 24 accounted tabs in a 12S1P topology. The boundary conditions for a cell were between the cell's surface and the ambient temperature, as calculated in Equation (15). For the module level, the heat convection transfer coefficient varied during testing time, and it was calculated by the software based on the air properties at the selected design (mass-flow speed, channel sizes, temperature, etc.). The model was solved with COMSOL software v5.5 using the MUMPS solver with a default physics-controlled unstructured tetrahedral mesh, as well as with the non-slip boundary conditions being imposed to the walls and the initial temperature being set at the ambient temperature i.e., 25 °C.

## 4. Experimental and Numerical Studies

The BTMS evaluations were performed at a 25 °C ambient temperature for a constant current discharge, as well as with maximum allowed C-rates (2 C), a discharge/charge cycle at the recommended rates (1 C), and a dynamic loading profile (WLTC). For each case, the single cell electrical validation is shown with the modeling voltage in comparison with

the experimentally obtained results. In addition, their relative error $V_{err}$ is used as a model accuracy indicator as follows:

$$V_{err} = \frac{V_{exp} - V_{batt}}{V_{exp}} * 100\%. \tag{21}$$

Furthermore, the single-cell temperature behavior was evaluated and the corresponding heat generation was obtained based on Equation (15). The analysis was continued for the multi-cell model by comparing the modeling to the experimental temperature behaviors, which was measured at two different locations. The first thermocouple was placed in the outer area of the first cell (noted as $T_1$) and the second (noted as $T_2$) between the fifth and sixth cells of the 12S1P module. Both were placed in the center of the cells, and, by these means, the thermal uniformity among the cells could be monitored and assessed.

For the module assessments, the initial SoC of the cells was 85% and this decreased by up to approximately 20% in order to bypass any of the balancing processes from the BMS. During the experimental implementation, a velocity of 1 m/s was measured via an anemometer, which corresponded to an approximately 0.012 m$^3$/s mass flow rate for a channel size $L_{cha}$ that was set at 60 mm.

### 4.1. Maximum Static Discharge

A 2 C constant current profile over the whole available SoC was loaded to the battery for single-level electrical validation.

### 4.1.1. Cell-Level Static Evaluation

The single-cell model voltage behavior is shown against the experimental behavior along with their relative errors in Figure 5. It was observed that the proposed model can map a high accuracy with the voltage behavior over the whole SoC range. Only a slight deviation occurs during the last steps of the discharge, and this is possibly due to the unexplored lithium diffusion processes that occur simultaneously in the cells [36], which could have been better captured with extra CPEs in the model. Nonetheless, for the proposed model, the relative error stayed below 4% over the whole experiment.



|      (a)      |      (b)      |
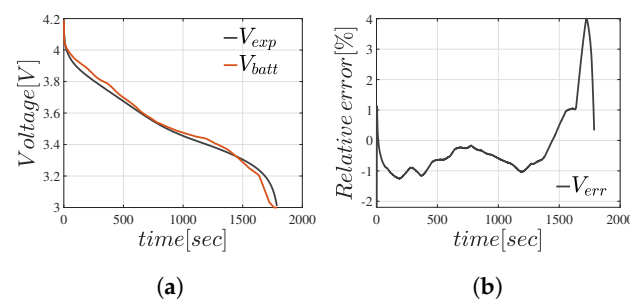
**Figure 5.** (**a**) Static single cell voltage behavior. (**b**) Relative error.

The thermal validation of the model can be seen through a comparison of the experimental with the simulation results. The temperature behavior for this case is shown in Figure 6 with the corresponding heat generation. To accord with the real conditions of the air flow in the thermal chamber, in a single-cell model, the heat transfer coefficient was set to 10 W/(m$^2$·K).

The abovementioned diffusion effect did not highly affect the temperature accuracy in the simulation. A good agreement was achieved over the whole experiment, which helped with verifying the proposed process and allowed it to proceed with multi-cell assessments.
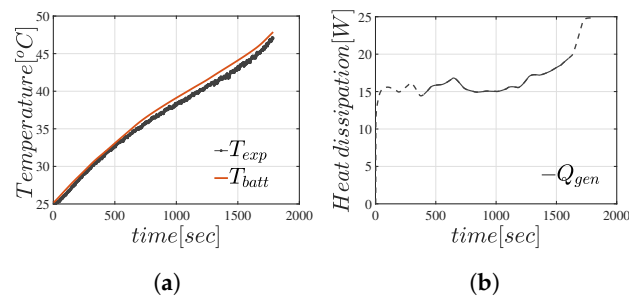
**Figure 6.** (**a**) Single cell temperature behavior at a constant current profile. (**b**) Heat generation.

### 4.1.2. Module-Level Static Validation

The module was validated for a static current with an initial SoC at approximately 85%, which was then discharged by up to 20%. Figure 6b shows, with solid lines, the heat generation input to the CFD model. The experimental and numerical results are shown at the locations of $T_1$ and $T_2$ in Figure 7. In the same figure, the blue line shows the behavior of a natural convention model (NC BTMS) without any cooling, and it was obtained from the numerical solution.
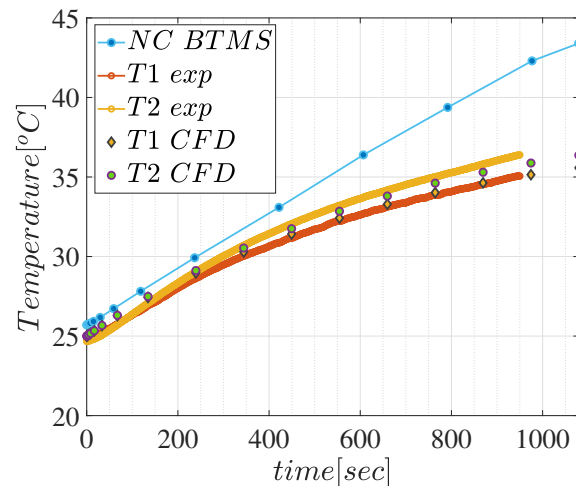


**Figure 7.** Constant current BTMS validation.

It was observed that the proposed BTMS model fit, with a good agreement, the experimental data and could keep the maximum temperature lower than 36 °C, which is approximately 9 °C lower than what was encountered with the NC-BTMS. Also, the heat uniformity was below 3 °C, which signifies the efficiency of the proposed air-based BTMS under this demanding loading. The selected battery module presented in Figure 8a is a result of the digitalized methodology over the various available designs with respect to inlet/outlet topology, cell spacing, etc. More details can be found in our previous publication [20]. The heat distribution at the end of the test profile is shown in Figure 8 for the proposed thermo-mechanical design (a), as well as the solution and natural convection (b), at the end (1200 s) of the discharge. The maximum temperature evolution was improved by approximately 10 °C, while the thermal uniformity among the cells was improved by approximately 4 °C with a maximum deviation of 1 °C (as can be further investigated here [20]).

(**a**)　　　　　　　　　　　　　　　　　(**b**)
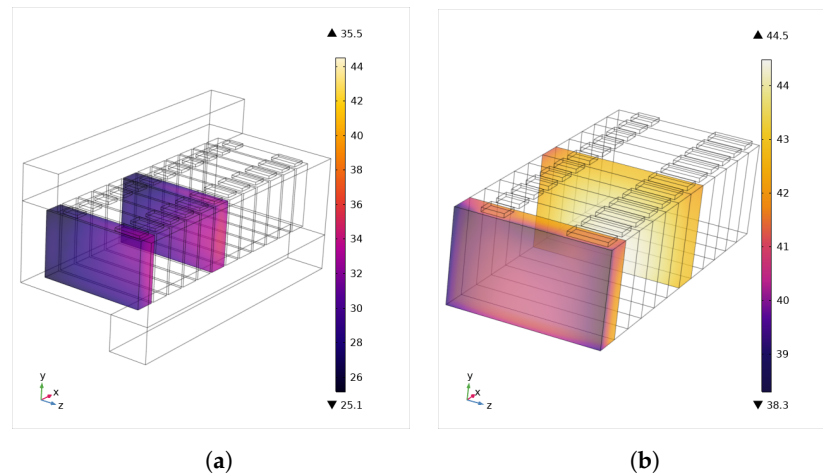
**Figure 8.** (**a**) The proposed BTMS. (**b**) The natural convection heat distribution.

### 4.2. Discharge–Charge Cycle

The current profile of a constant discharge–charge cycle that was applied on both topologies is shown in Figure 9.

The cells were charged to an approximate 85% SoC, and they were then discharged with 1 C for 2000 s. They experienced an immediate charge with the same C-rate until the SoC had reached the initial level.
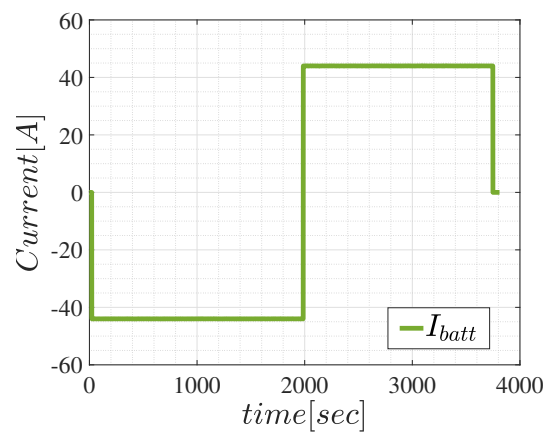


**Figure 9.** The discharge-charge cycle with a 1 C rate.

### 4.2.1. Cell-Level Cycle Evaluation

The experimental and modeling voltages are shown with the respective relative errors in Figure 10.



(**a**)　　　　　　　　　　　　　　　　　(**b**)
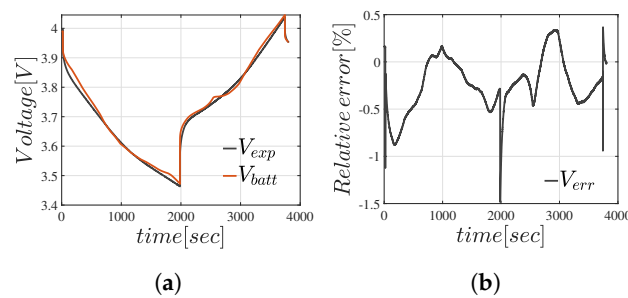
**Figure 10.** (**a**) The discharge-charge single cell voltage behavior. (**b**) The relative error.

The activation and concentration polarization effects are shown with higher and lower time constants in the model. They can be tracked with high accuracy, as indicated by the

relative error that stayed below 1.5% for the whole test. The corresponding temperature behavior, validation, and heat generation are illustrated in Figure 11.
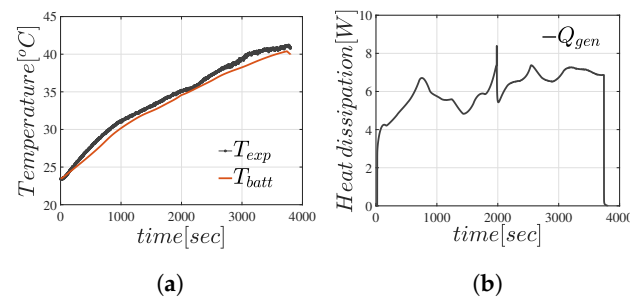


**Figure 11.** (**a**) The single cell temperature behavior with a current cycle. (**b**) Heat generation.

Compared to the previous case, it was observed that the voltage could be realized with a single diffusion element. Hence, a good thermal agreement was achieved, whereas it was also observed that the charge resistance was slightly higher than discharge, as indicated by the heat dissipation curve.

### 4.2.2. Module-Level Cycle Validation

A time-dependent heat generation was supplied to the CFD model. Even though, for the two current pulses, the test time was higher and the heat generation was based on the impedance data from both charge and discharge profiles, the temperature behavior can be tracked with a high accuracy, as shown in Figure 12.
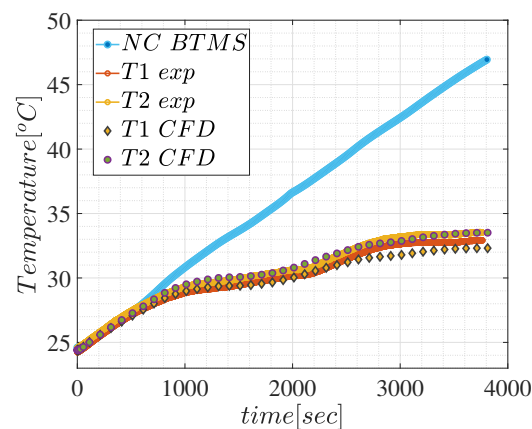


**Figure 12.** The discharge–charge current BTMS validation.

Also, the proposed module was capable of keeping the maximum temperature below 35 °C when compared to the NC-BTMS, while the heat uniformity was established with thermocouples $T_1$ and $T_2$, as well as by the good agreement between the experimental and CFD values.

### 4.3. Dynamic Loading—WLTC

In the last study case, the WLTC dynamic current profile, as shown in Figure 13, was applied to the cells. It was based on a mixture of low and more demanding current pulses with the maximum C-rate being limited at 1.5 C (60 A).

The applied profile was composed of four consecutive WLTC cycles that discharged the cells for an approximate 60% SoC. Similar to previous cases, to avoid the balancing effects of the BMS, the initial SoC was set at around 85% and the test was conducted in 25 °C ambient conditions.
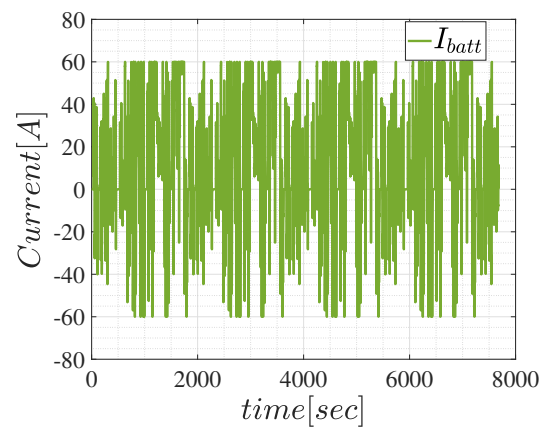
**Figure 13.** The dynamic cycle based on the WLTC profile.

### 4.3.1. Cell-Level WLTC Evaluation

The R-(BVE//CPE) branch was found to be very efficient for the fast dynamics that were mainly accounted for in this profile. Throughout the whole test, the relative error did not exceed 0.5% of the actual voltage value, as shown in Figure 14.

Hereafter, the proposed electro-thermal model captured the temperature behavior with high accuracy, the corresponding heat generation of which is shown in Figure 15.



(**a**)         (**b**)
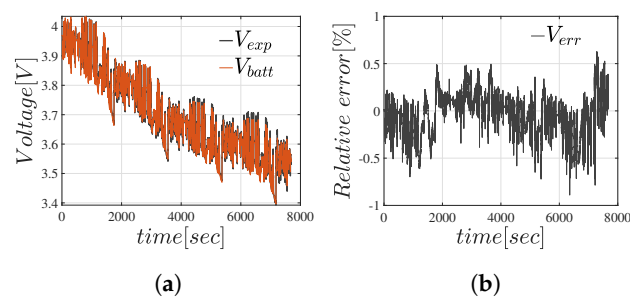
**Figure 14.** (**a**) The dynamic profile single cell voltage behavior. (**b**) The relative error.



(**a**)         (**b**)
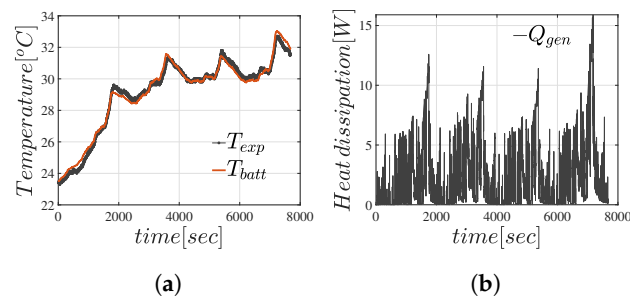
**Figure 15.** (**a**) The single cell temperature behavior with a WLTC profile. (**b**) The heat generation.

### 4.3.2. Module-Level WLTC Validation

The dynamic profile was applied to the 12S1P air-based module, and the experiment data when compared against the CFD are shown in Figure 16.

A good agreement was achieved both on the maximum temperature and heat distribution for the proposed module. It was observed that the consecutive current cycles could elevate the maximum temperature at the end of the experiment (approx. 20% SoC) to 38 °C. Based on the NC-BTMS model, which is indicated with the blue line, the temperature had an increasing rate of change. This could lead to surpassing the safety window if no cooling solution is applied. However, the proposed BTMS showed a stable thermal trend without exceeding 28 °C.
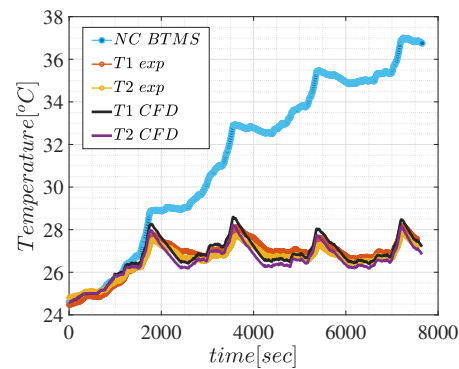
**Figure 16.** The dynamic current BTMS validation.

## 5. BTMS Cost-Effectiveness Study

The proposed module was strategically optimized, as detailed in this section. For this purpose, the validated numerical model was used to help visualize and predict the temperature behavior when using various structural designs.

### 5.1. The Inlet Coolant Flow Rate

Different inlet coolant flow rates were evaluated to help determine the influence on the temperature evolution of the proposed BTMS. The coolant was set at the same temperature as the ambient, i.e., 25 °C, whereas, for the evaluation and validation steps, a 0.012 $m^3$/s flow speed was selected. Figure 17a demonstrates the temperature contours of 0.01 $m^3$/s to 0.04 $m^3$/s. It was observed that the temperature declined when increasing the flow rate. With the coolant rate increasing from 0.01 $m^3$/s to 0.04 $m^3$/s, the maximum temperature dropped to 8 °C at the end of a 2 C static discharge loading, and this was as a result of the enhanced convective heat transfer between the cells and the air coolant. However, the increased flow rate could proportionally increase the hot spots on the cells and deteriorate the uniformity in the module. The local hotter zones could create a higher localized negative aging effect on the cells as a faster degradation was expected at those points. Operations outside the SoA can jeopardize the safety and performance of the module. To find the optimal flow rate, the pressure drop was plotted with the temperature behavior, as shown in Figure 17b. It was evident that the higher the flow rate, the steeper the temperature drop and the cooling speed. The results depicted in the figure verified the fact that a non-linear relationship was obtained between the coolant rate and the pressure drop. To balance between the pressure loss and the thermal management, a mass flow rate at the intersection of those curves, at approximately 0.023 $m^3$/s, was selected.



(**a**)

(**b**)
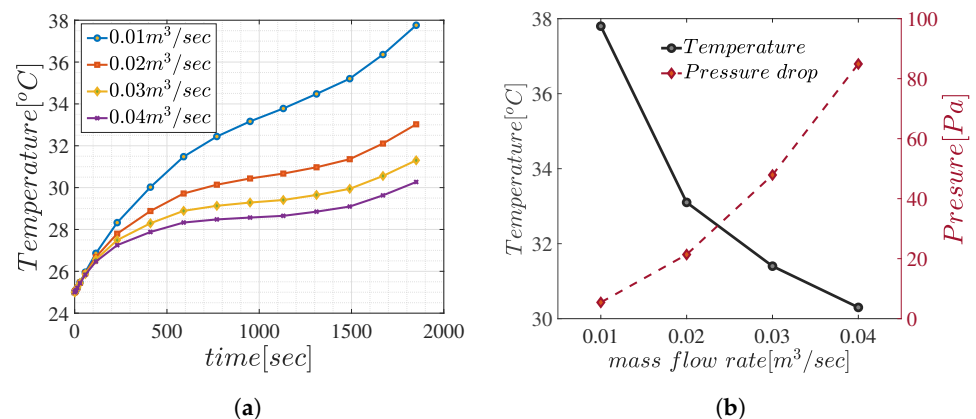
**Figure 17.** (**a**) Temperature behaviors. (**b**) The pressure drop at various mass flow rates.

## 5.2. Channel Size

The design of the channels' input and output played an important role in managing the temperature and pressure losses of the proposed BTMS. In this part, the evaluation was performed with channel sizes of 20 mm to 60 mm. The symmetries of the input and output channels were recorded, whereas, for the main case study and experimental validation, the channels were designed with an approximately 55 mm size. It is shown in Figure 18 that, from increments in the channel size, the monitored maximum temperature decreased by up to 2 °C. On the other hand, the pressure drop showed a sharp increase that was up to four times higher as the channel size increased. The study was performed with the previously optimized mass flow rate (0.023 m$^3$/s).
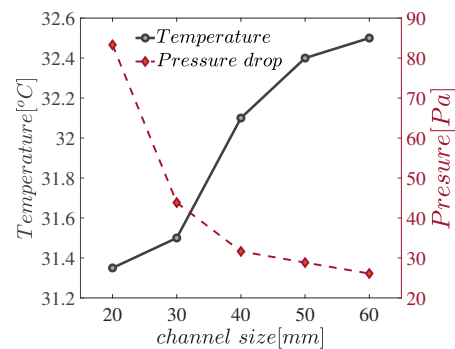


**Figure 18.** The pressure drop and maximum temperature at various channel sizes.

Hence, the optimized BTMS was to be implemented with a trade-off value, for which the temperature and the cost could be balanced, of approximately 30 mm for the channel size.

## 5.3. Cell-to-Cell Space

The last key parameter to be optimized based on the pressure drop and the heat distribution was the cell-to-cell distance. The optimal flow rate and channel size obtained in previous sections were now accounted for. In the following Figure 19, it is clearly shown that, when increasing the cell's intermediate distances, the cell's maximum temperature at the end of a 2 C discharge process was decreased by up to approximately 4 °C. It was also observed that the drop decreased from 75 Pa to 45 Pa. This meant that, by increasing the cell-to-cell distance, not only did the temperature decline, but a pressure drop reduction was also observed, as illustrated in Figure 19b. Nonetheless, increasing the distance by more than 4 mm could lead to extra costs when the temperature is not proportionally dropped. An approximate 4 mm distance was hence selected as the optimized value for the proposed BTMS.



(a)

**Figure 19.** *Cont.*

**(b)**
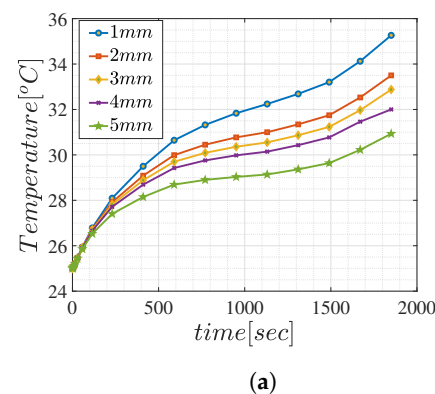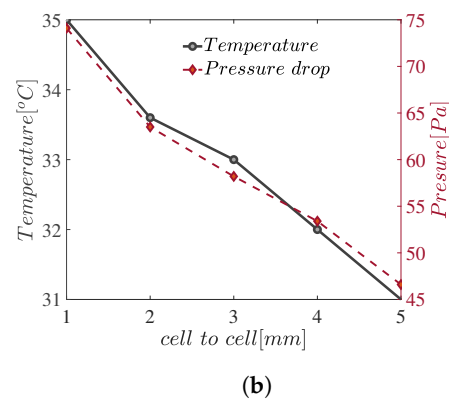
**Figure 19.** (**a**) Temperature behaviors. (**b**) The pressure drop at various cell-to-cell distances.

## 6. Discussion

While the design optimization method presented in this work can significantly enhance the performance, efficiency, and safety of Li-ion battery systems, several constraints may affect its broader adoption across diverse applications. In this section, we try to elaborate on the challenges that might arise during the design optimization method for the purposes of future consideration and wider adoption. The first challenge was computational power and efficiency. We demonstrated that our method required a non-stop optimization process of approximately 5 days [20]. Hence, the multi-objective design optimization methods implemented in 3D environments involved complex mathematical models, simulations, and algorithms, which were used to analyze various design parameters and optimize performance criteria, as was presented in our work. Implementing these methods requires substantial computational resources, including high-performance computing systems, advanced software tools, and expertise in the numerical methods. With the trade-off that can be made on the various modeling approaches, the modeling accuracy of the battery systems can vary significantly. An accurate battery behavior is essential for effective design optimization. However, developing accurate battery models that can capture the internal electrochemical processes, the thermal behavior at various conditions, and mechanical interactions can be challenging. Furthermore, the validation of these models against experimental data is crucial but often time-consuming and costly. Such model inaccuracies or uncertainties can lead to suboptimal designs or unexpected performance issues, thereby undermining the reliability and effectiveness of design optimization methods. This is one of the main purposes that validations were presented after the construction of the proposed module design, as well as after further analyses, in the current work. Moreover, a global implementation of the proposed method should concern the numerous interdependent parameters, including the cell chemistry, geometry, materials, thermal management strategies, and operating conditions of the various cell chemistries and formats. Exploring this vast design space to identify optimal solutions while considering trade-offs between conflicting objectives might be challenging. An extra important constraint that one should consider is that the optimized designs generated through computational methods may not always be readily manufacturable or scalable to large-scale production. Design constraints imposed by manufacturing processes, material availability, supply chain logistics, and cost considerations may limit the practical feasibility of implementing optimized designs in real-world applications. Bridging the gap between design optimization and manufacturability is essential for ensuring the broader adoption of the proposed method.

## 7. Conclusions and Future Work

In this work, the performance of an air-cooled, battery thermal management system (BTMS) was studied for a battery module composed of 12 high-energy, prismatic Li-ion cells connected in series.

A physically meaningful electrical model was built based on fractional-order calculus, which helped to map the impedance of the cells with high accuracy. The single cell electrical model was coupled to a thermal branch, and it was evaluated with three different current profiles, a maximum static discharge current, a discharge–charge cycle, and a consecutive dynamic profile. A good agreement between the modeling and the experimental values was achieved, and this was underlined with the low relative errors obtained in each study case. Hence, the heat generation was derived and supplied to an efficient three-dimensional model, which was also validated against the experimental results obtained from various current profiles. The roles of natural convection (NC-BTMS) and forced convection were studied separately for the proposed BTMS under intense static and dynamic loads.

By optimizing the key performance parameters, such as the mass flow velocity and the channel size, one can conclude that their increment leads to a maximum temperature reduction. Also, the cell-to-cell distance increase had a reverse impact on the temperature and the pressure drop. By these means, the thermal management of the proposed architecture was enhanced while the pressure drop was kept at a minimum range.

A significant improvement can be concluded from this study—one that is related to the overall physics-based structural optimization of the battery modules. The coupling of high-fidelity models with global optima multi-objective algorithms could consider the following: (1) a wider design space with many objectives (which is proven in this study, i.e., that co-design electrical-thermal and mechanical objectives can be solved at the same time); (2) the optimization steps that are evaluated can be significantly increased when compared to user-based or single-objective solutions (i.e., the sampling time related to the computational time and step-time related to the amount of derived solutions that could be set accordingly); and (3) the optimization results presented in this paper are accurate versus the real-life experiments for various loading scenarios.

The method we have presented here was studied with a air-cooled battery module design. To optimize this design, we used a multi-objective optimization that used four objectives and several constraints, as presented in Equation (1). By changing the cost functions and the constraints, the use case could be adapted to other designs and battery configurations, such as when investigating the liquid channel sizes, mass flows, and pressure drops, in order to provide the most suitable solutions. We are currently working on such investigations, and future publications will present the performance of the proposed methods to a different design set. Forthcoming works might include a study on the proposed BTMS when it is applied to a higher energy and power battery pack, as well as an evaluation of different thermal management solutions for different objectives and constraints.

**Author Contributions:** Conceptualization, T.K.; methodology, T.K.; software, T.K.; validation, T.K. and M.S.H.; formal analysis, T.K.; investigation, T.K.; resources, M.B. and J.V.M.; data curation, T.K.; writing—original draft preparation, T.K. and M.S.H.; writing—review and editing, T.K. visualization, T.K.; supervision, P.V.D.B. and M.B.; project administration, J.V.M.; funding acquisition, M.B. All authors have read and agreed to the published version of the manuscript.

**Data Availability Statement:** The datasets presented in this article are not readily available because the data are part of an ongoing study.

**Conflicts of Interest:** The authors declare no conflicts of interest.

## References

1. Deng, J.; Bae, C.; Denlinger, A.; Miller, T. Electric Vehicles Batteries: Requirements and Challenges. *Joule* **2020**, *4*, 511–515. [CrossRef]
2. Kebede, A.A.; Hosen, M.S.; Kalogiannis, T.; Behabtu, H.A.; Assefa, M.Z.; Jemal, T.; Ramayya, V.; Van Mierlo, J.; Coosemans, T.; Berecibar, M. Optimal sizing and lifetime investigation of second life lithium-ion battery for grid-scale stationary application. *J. Energy Storage* **2023**, *72*, 108541. [CrossRef]

3.    Peters, J.F.; Baumann, M.; Zimmermann, B.; Braun, J.; Weil, M. The environmental impact of Li-Ion batteries and the role of key parameters—A review. *Renew. Sustain. Energy Rev.* **2017**, *67*, 491–506.

4.    Balali, Y.; Stegen, S. Review of energy storage systems for vehicles based on technology, environmental impacts, and costs. *Renew. Sustain. Energy Rev.* **2021**, *135*, 110185. [CrossRef]

5.    Gandoman, F.H.; Jaguemont, J.; Goutam, S.; Gopalakrishnan, R.; Firouz, Y.; Kalogiannis, T.; Omar, N.; Van Mierlo, J. Concept of reliability and safety assessment of lithium-ion batteries in electric vehicles: Basics, progress, and challenges. *Appl. Energy* **2019**, *251*, 113343.

6.    Rezvanizaniani, S.M.; Liu, Z.; Chen, Y.; Lee, J. Review and recent advances in battery health monitoring and prognostics technologies for electric vehicle (EV) safety and mobility. *J. Power Sources* **2014**, *256*, 110–124. [CrossRef]

7.    Song, W.; Chen, M.; Bai, F.; Lin, S.; Chen, Y.; Feng, Z. Non-uniform effect on the thermal/aging performance of Lithium-ion pouch battery. *Appl. Therm. Eng.* **2018**, *128*, 1165–1174. [CrossRef]

8.    Iraola, U.; Aizpuru, I.; Gorrotxategi, L.; Segade, J.M.C.; Larrazabal, A.E.; Gil, I. Influence of voltage balancing on the temperature distribution of a Li-ion battery module. *IEEE Trans. Energy Convers.* **2015**, *30*, 507–514. [CrossRef]

9.    Arora, S. Selection of thermal management system for modular battery packs of electric vehicles: A review of existing and emerging technologies. *J. Power Sources* **2018**, *400*, 621–640. [CrossRef]

10.   Xie, P.; Jin, L.; Qiao, G.; Lin, C.; Barreneche, C.; Ding, Y. Thermal energy storage for electric vehicles at low temperatures: Concepts, systems, devices and materials. *Renew. Sustain. Energy Rev.* **2022**, *160*, 112263. [CrossRef]

11.   Akinlabi, A.A.; Solyali, D. Configuration, design, and optimization of air-cooled battery thermal management system for electric vehicles: A review. *Renew. Sustain. Energy Rev.* **2020**, *125*, 109815. [CrossRef]

12.   Peng, X.; Cui, X.; Liao, X.; Garg, A. A thermal investigation and optimization of an air-cooled lithium-ion battery pack. *Energies* **2020**, *13*, 2956. [CrossRef]

13.   Park, H. A design of air flow configuration for cooling lithium ion battery in hybrid electric vehicles. *J. Power Sources* **2013**, *239*, 30–36. [CrossRef]

14.   Chen, K.; Wang, S.; Song, M.; Chen, L. Configuration optimization of battery pack in parallel air-cooled battery thermal management system using an optimization strategy. *Appl. Therm. Eng.* **2017**, *123*, 177–186. [CrossRef]

15.   Xie, J.; Ge, Z.; Zang, M.; Wang, S. Structural optimization of lithium-ion battery pack with forced air cooling system. *Appl. Therm. Eng.* **2017**, *126*, 583–593. [CrossRef]

16.   Chen, K.; Song, M.; Wei, W.; Wang, S. Structure optimization of parallel air-cooled battery thermal management system with U-type fl ow for cooling ef fi ciency improvement. *Energy* **2018**, *145*, 603–613. [CrossRef]

17.   Liu, Y.; Zhang, J. Design a J-type air-based battery thermal management system through surrogate-based optimization. *Appl. Energy* **2019**, *252*, 1–13. [CrossRef]

18.   Chen, K.; Wu, W.; Yuan, F.; Chen, L.; Wang, S. Cooling efficiency improvement of air-cooled battery thermal management system through designing the flow pattern. *Energy* **2019**, *167*, 781–790. [CrossRef]

19.   Li, M.; Liu, Y.; Wang, X.; Zhang, J. Modeling and optimization of an enhanced battery thermal management system in electric vehicles. *Front. Mech. Eng.* **2019**, *14*, 65–75. [CrossRef]

20.   Kalogiannis, T.; Akbarzadeh, M.; Hosen, M.S.; Behi, H.; De Sutter, L.; Jin, L.; Jaguemont, J.; Van Mierlo, J.; Berecibar, M. Effects analysis on energy density optimization and thermal efficiency enhancement of the air-cooled Li-ion battery modules. *J. Energy Storage* **2022**, *48*, 103847. [CrossRef]

21.   Kalogiannis, T.; Hosen, M.S.; Gandoman, F.H.; Sokkeh, M.A.; Jaguemont, J.; Berecibar, M.; Van Mierlo, J. Multi-objective particle swarm optimization and training of datasheet-based load dependent lithium-ion voltage models. *Int. J. Electr. Power Energy Syst.* **2021**, *133*, 107312. [CrossRef]

22.   Barai, A.; Uddin, K.; Dubarry, M.; Somerville, L.; McGordon, A.; Jennings, P.; Bloom, I. A comparison of methodologies for the non-invasive characterisation of commercial Li-ion cells. *Prog. Energy Combust. Sci.* **2019**, *72*, 1–31.

23.   Akbarzadeh, M.; Kalogiannis, T.; Jaguemont, J.; He, J.; Jin, L.; Berecibar, M.; Van Mierlo, J. Thermal modeling of a high-energy prismatic lithium-ion battery cell and module based on a new thermal characterization methodology. *J. Energy Storage* **2020**, *32*, 101707. [CrossRef]

24.   Wang, B.; Li, S.E.; Peng, H.; Liu, Z. Fractional-order modeling and parameter identification for lithium-ion batteries. *J. Power Sources* **2015**, *293*, 151–161. [CrossRef]

25.   Brivio, C.; Musolino, V.; Merlo, M.; Ballif, C. A Physically-Based Electrical Model for Lithium-Ion Cells. *IEEE Trans. Energy Convers.* **2019**, *34*, 594–603. [CrossRef]

26.   Wang, Y.N.; Chen, Y.Q.; Liao, X.Z. State-of-art survey of fractional order modeling and estimation methods for lithium-ion batteries. *Fract. Calc. Appl. Anal.* **2020**, *22*, 1449–1479. [CrossRef]

27.   Xiong, R.; Tian, J.; Shen, W.; Sun, F. A Novel Fractional Order Model for State of Charge Estimation in Lithium Ion Batteries. *IEEE Trans. Veh. Technol.* **2019**, *68*, 4130–4139. [CrossRef]

28.   Xiong, R.; Tian, J. A comparative study on fractional order models for voltage simulation of lithium ion batteries. In Proceedings of the 2019 IEEE 89th Vehicular Technology Conference, Kuala Lumpur, Malaysia, 28 April–1 May 2019; pp. 1–5. [CrossRef]

29.   Mawonou, K.S.; Eddahech, A.; Dumur, D.; Beauvois, D.; Godoy, E. Improved state of charge estimation for Li-ion batteries using fractional order extended Kalman filter. *J. Power Sources* **2019**, *435*, 226710. [CrossRef]

30.  Petras, I. *Fractional-Order Nonlinear Systems. Modeling, Analysis and Simulation*; Higher Education Press: Beijing China; Springer: Berlin/Heidelberg, Germany, 2011.
31.  Zhu, J.; Sun, Z.; Wei, X.; Dai, H. Studies on the medium-frequency impedance arc for Lithium-ion batteries considering various alternating current amplitudes. *J. Appl. Electrochem.* **2016**, *46*, 157–167. [CrossRef]
32.  Farmann, A.; Sauer, D.U. Comparative study of reduced order equivalent circuit models for on-board state-of-available-power prediction of lithium-ion batteries in electric vehicles. *Appl. Energy* **2018**, *225*, 1102–1122. [CrossRef]
33.  Kalogiannis, T.; Jaguemont, J.; Omar, N.; Van Mierlo, J.; Van den Bossche, P. A comparison of internal and external preheat methods for NMC batteries. *World Electr. Veh. J.* **2019**, *10*, 18. [CrossRef]
34.  Chen, K.; Chen, Y.; Li, Z.; Yuan, F.; Wang, S. Design of the cell spacings of battery pack in parallel air-cooled battery thermal management system. *Int. J. Heat Mass Transf.* **2018**, *127*, 393–401. [CrossRef]
35.  Akbarzadeh, M.; Jaguemont, J.; Kalogiannis, T.; Karimi, D.; He, J.; Jin, L.; Xie, P.; Van Mierlo, J.; Berecibar, M. A novel liquid cooling plate concept for thermal management of lithium-ion batteries in electric vehicles. *Energy Convers. Manag.* **2021**, *231*, 113862. [CrossRef]
36.  Gantenbein, S.; Weiss, M.; Ivers-Tiffée, E. Impedance based time-domain modeling of lithium-ion batteries: Part I. *J. Power Sources* **2018**, *379*, 317–327. [CrossRef]